Technical University of Denmark

Environmental TEM study of the dynamic nanoscaled morphology of NiO/YSZ during reduction

Simonsen, Søren Bredmose; Agersted, Karsten; Hansen, Karin Vels; Jacobsen, Torben; Wagner, Jakob Birkedal; Hansen, Thomas Willum; Kuhn, Luise Theil

Link back to DTU Orbit

DTU Library
Technical Information Center of Denmark

Environmental TEM study of the dynamic nanoscaled morphology of NiO/YSZ during reduction

Søren Bredmose Simonsen[a,*], Karsten Agersted[a], Karin Vels Hansen[a], Torben Jacobsen[a], Jakob Birkedal Wagner[b], Thomas Willum Hansen[b], Luise Theil Kuhn[a]

[a]Department of Energy Conversion and Storage, Technical University of Denmark, DK-4000 Roskilde, Denmark
[b]Center for Electron Nanoscopy, Technical University of Denmark, DK-2800 Kgs. Lyngby, Denmark

*Corresponding author, email address: sobrs@dtu.dk, phone: +45 20 12 06 11 (Søren Bredmose Simonsen)

Keywords:

Nickel oxide reduction, NiO, YSZ, SOFC, SOEC, in situ TEM, ETEM, autocatalysis

Abstract

The reduction of a metal oxide is often a critical preparation step for activating catalytic behavior. This study addresses the reduction process of NiO in pure form and in a composite of NiO/yttria-stabilized zirconia (YSZ) in hydrogen relevant for solid oxide electrochemical cells by comparing results from environmental transmission electron microscopy (ETEM) with thermogravimetric analysis (TGA). The temperature dependent reduction profiles obtained from TGA confirm an inhibitive effect from YSZ on the NiO reduction. The ETEM images show the growth of Ni in decaying NiO and reveal the nanoscale morphological changes such as pore formation in NiO above 280°C and densification and collapse of the pore structures above 400°C. The accelerated Ni front in NiO illustrates the autocatalysis of the reaction. A rapid temperature ramping from room temperature to 780°C in hydrogen in 1 second resulted in immediate morphological changes at the nanoscale from dense NiO to dense Ni. The analysis suggests that the inhibitive effect of YSZ on the NiO reduction reaction is not due to a direct local interaction between YSZ and NiO, but instead due to gas and/or mass transport limitations.

1. Introduction

The reduction of metal oxides is a typical step in the preparation of the active metal surfaces for various catalyst systems. Conditions of the reduction process, such as temperature, reduction time, gas composition, gas flow and pressure, are important for optimizing the catalyst performance [1,2].

Understanding the metal oxide reduction process is therefore important in order to be able to optimize the catalyst activity. The reduction of nickel-based catalysts used for e.g. oxidation [3], methanation [4] and ammonia decomposition [5] has been extensively studied [2,6-16]. The reduction of NiO with H_2 occurs without any intermediate phase [8] and can be described by the relatively simple formula:

$$NiO\ (s) + H_2\ (g) \rightarrow Ni\ (s) + H_2O\ (g) \tag{1}$$
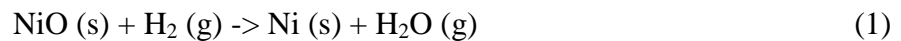
The loss of oxygen during reduction leads to a volume decrease by 41 % resulting in a restructuring of the overall morphology of the solid and can lead to pore formation in the Ni [17-19]. A delay in the reduction onset, a so-called incubation or induction period is reported, which decreases with reaction temperature [6,8,10,12] and increasing number of defects on the NiO surface [10]. It has been suggested that dissociative adsorption of hydrogen, which is a necessary initiation step for the NiO reduction, preferentially takes place at NiO surface oxygen vacancies [8,10]. The reduced Ni surface will act as a catalyst for dissociative H_2 adsorption and it has been suggested that the reduction of NiO will be autocatalytically accelerated in the vicinity of a Ni surface [6]. On the contrary, the produced H_2O influences the reaction rate negatively, possibly by poisoning of the active sites for H_2 adsorption [6, 18]. In addition it has been reported that the reaction rate scales with the H_2 pressure [8,10,17].

Ni catalysts are often integrated into an oxide matrix and for such systems the reduction of Ni oxide can be slower than for the pure NiO [7,12]. An important example is the porous composite of Ni and yttria-stabilized zirconia (YSZ), which is the state-of-the-art anode in commercial solid oxide fuel cells (SOFC) and cathode in solid oxide electrolysis cells (SOEC) [11-16]. In these electrochemical cells Ni simultaneously acts as an electron conductor and catalyst for splitting the adsorbed reactive gases, while YSZ acts as an oxygen ion conductor. The porous Ni/YSZ is typically prepared from powder mixtures of NiO and YSZ [13,14,16], sintered into a dense structure and finally reduced during start-up of the SOFCs/SOECs, typically around 800°C [13,15,16]. The overall performance of SOFCs/SOECs depends on the initial reduction step and the related morphology [12,20] and several studies have focused on the reduction of NiO in mixtures with YSZ [12,15,16,19,20]. It is reported that YSZ inhibits the reduction of NiO [11,12,16], but the reason for the inhibitive effect of YSZ is not clear. Linear kinetics in the reduction of dense NiO/YSZ samples at temperatures below 700°C suggests that the reaction is interface controlled and therefore not limited by gas transport in the produced porous Ni [13,16,18]. On the other hand,

YSZ has been suggested to act as transport barrier for the reaction front inside the NiO/YSZ matrix [12]. Increasing sintering temperatures leads to a stronger inhibitive effect of YSZ, and the effect has therefore previously been explained by formation of NiO crystallites incorporated in YSZ and formation of a metastable solid solution of NiO in YSZ [16]. It has also been suggested that the reduction rate at the NiO-YSZ interfaces is relatively low due to a NiO-YSZ chemical interaction [16] or due to a slow Ni nucleation [12].

Techniques, such as thermogravimetric analysis (TGA) [12,14], thermomechanical analysis (TMA) [14], temperature programmed reduction (TPR) [11], X-ray diffraction (XRD) [10,11,15], X-ray photoelectron spectroscopy (XPS) [8,10] and Auger spectroscopy [8,10] have given significant insight into the NiO reduction process. In addition, local information has been obtained using post mortem electron microscopy [12,13,14,17,18]. However, nanoscale dynamics, such as initiation of the reduction, crystal growth/decay or morphological changes of NiO and Ni during reduction can only be indirectly probed with these techniques. It can also be difficult to separate the different structural parameters that simultaneously influence the reduction process, such as local composition, particles sizes, mobility of the solids and pathways for gas transport in the samples [17,18]. ETEM offers a localized study with atomic resolution in a gas environment at elevated temperatures [21-24]. ETEM has been used to study the NiO reduction reaction at the nanoscale [19,25-28] and has given insight into e.g. the mobile species (Ni-atoms [25] or O-atoms [19]) and the initial Ni formation at the NiO surfaces [24].

The present work is a comparative study of the reduction of pure NiO and NiO/YSZ with a) TGA to describe the overall temperature dependency of the reaction for macroscopic samples and with b) ETEM to probe the sample at the nanoscale during exposure to H_2 at elevated temperatures. The goal of the study is firstly to address the apparent inhibitive influence from YSZ on the NiO reduction and secondly to describe the morphological changes of the NiO/YSZ during reduction at different temperature ramping rates for temperatures up to 780°C.

2. Experimental

2.1 Catalyst preparation

An SOFC anode (SOEC cathode) consisting of 56 wt.% NiO and 44 wt.% YSZ with 8 mol% yttria was prepared by tape casting from mixed powder of NiO (Novamet Specialty Products Corp.) and YSZ (Tosoh Corporation) as described in detail in reference [29]. A reference sample was prepared

by tape casting the pure YSZ. An additional reference sample was prepared by die pressing a pellet from the pure NiO powder. All of these samples were sintered in air at 1350°C for 3 hours. In one experiment the dense NiO/YSZ sample was used without further preparations, but for other experiments the samples were ground into a fine powder in a mortar. In addition, the raw NiO powder was used as a non-sintered reference sample.

2.2 Catalyst characterization

TGA was performed on all samples on a Netzsch STA 409CD Thermobalance. The powder samples were spread out on the surface of a wok-type sample holder mounted vertically in the test chamber. 50 mg of YSZ and NiO/YSZ powder was used. 30 mg of the pure NiO powder was used, to assure a similar amount of NiO was used in both sample types. In addition to the powder samples, a piece of 30 mg of the sintered dense NiO/YSZ sample was placed in a flat holder with a diameter of 17 mm (Netzsch 445.240). The TGA experiments were performed in a flow of 50 Nml/min 9% H_2/N_2 (Air Liquide: H4.6; N6.0). The temperature was initially ramped from room temperature to 150°C at 10°C/min and held at this temperature for 2 hours to dry the samples prior to the actual reduction experiment. The reduction experiment was performed by ramping the temperature to 1200°C at 1°C/min.

Using a JEOL 3000F equipped with a 300kV FEG, a scanning unit (STEM) and a high-angle annular dark-field (HAADF) detector, ex situ STEM of the NiO/YSZ powder was carried out to determine the spatial distribution of the different elements in the sample at the nanoscale. Energy-dispersive X-ray spectroscopy (EDS) was carried out for compositional analysis by using an Oxford Instruments detector with an ultra-thin window. The analysis was performed using the Inca software. The ground powder was dispersed in ethanol and a droplet of the suspension was placed on a standard TEM copper grid.

The ETEM experiments were performed using a Titan 80-300 (FEI) electron microscope equipped with a differentially pumped environmental cell [30]. The microscope was operated with a primary electron energy of 300 keV. In the electron microscope, the powder samples were exposed to 2 mbar H_2 (AGA 6.0). The powder samples were ground with ethanol and droplets of the suspension were deposited on the surface of MEMS thermal E-chips (Protochips Inc.) and the samples were allowed to dry in air at room temperature before inserting the TEM holder. The chips used for the experiments were either with or without a carbon support. The chips were mounted in an Aduro 300

heating holder (Protochips Inc.) facilitating the heating of the samples in the gaseous environment. The temperature calibration of the heating holder is described in detail in the supplementary materials appendix A.

2.3 Critical remarks on the ETEM analysis

Before performing the actual reduction experiments it is necessary to determine whether artifacts are induced by the electron beam. Indeed it has been reported that NiO can be reduced by a focused 100kV electron probe in vacuum [9]. The NiO/YSZ sample was exposed to 2 mbar H_2 and a constant exposure to the electron beam with a beam current density of ca. 600 e^-/nm^2s for 30 min at room temperature. No structural changes of the NiO/YSZ were observed after this treatment, except that a layer of amorphous carbon builds up on the sample surface. The actual reduction experiments were performed at approximately the same beam current density, but with a lower total dose since the electron beam was blanked between image acquisitions. For the longest experiment the estimated total electron beam exposure was 15 min. In addition, comparison of areas followed over time with previously unexposed areas showed no characteristic structural differences. It is therefore unlikely that the dominating structural changes of the samples during the reduction experiments are due to the electron beam.

Since the TEM images are two-dimensional projections of the three-dimensional sample, the TEM image analysis can be challenging. For the present powder samples, it is easier to observe the initiation of the reduction process in thin regions and at the edges of the particles than at thicker regions and at surfaces normal to the electron beam. Also, overlapping NiO and YSZ grains with no contact could be mistaken for real NiO-YSZ interfaces. Further, since the sample temperature is controlled via the heat conducting support, heat gradients from the support and out through the sample cannot be ruled out. In addition, some of the sintered NiO-YSZ interfaces are possibly broken during sample preparation and it is not possible to determine with certainty whether an observed interface represents a sintered NiO-YSZ interface or NiO and YSZ particles bound by van der Waal forces. Two strategies in the analysis are followed to compensate for these issues: 1) For the image analysis, several imaged areas are compared to increase the probability of studying the sintered interfaces and variations of sample geometry. Specifically, six different areas with one or more NiO-YSZ interfaces were analyzed. 2) The ETEM image analysis, focusing on relatively few NiO-YSZ grains and interfaces, is compared to the ETEM diffraction analysis, which is based on a larger sample area (ca. 15 μm^2) with many NiO-YSZ grains and interfaces.

3. Results

3.1 TGA results

From TGA the temperature dependencies of the NiO reduction reaction were obtained (Fig. 1). The mass of the non-sintered NiO powder (Fig. 1, full black line) decreases relatively fast above 300°C. This is interpreted as loss of oxygen by referring to the reaction described by Eqn. 1. At 350°C, the non-sintered NiO powder has lost 85% of its oxygen, the reduction reaction rate (the slope of the curve) slows down and the mass decreases until reaching 79% of the initial mass at ca. 800°C, corresponding to full reduction. The trend of the sintered NiO powder (Fig. 1, dashed black line) is similar to the non-sintered powder, but with a slightly higher initial reduction temperature. According to images recorded by scanning electron microscopy (not presented) the mean particle size of 100 random particles for the sintered NiO powder is 3 μm in diameter, while 0.7 μm for the non-sintered NiO powder. Since the total NiO surface area depends on the mean particle size, a lower reduction temperature could have been expected for the non-sintered powder, but it is observed that the size effect is relatively weak.

Similar to the pure NiO samples, full reduction of the mixed NiO/YSZ powder is reached at 800°C, but the reduction process is generally slower (Fig. 1 full grey line). The onset temperature is ca. 280°C, which is slightly below that of pure NiO powders. The pure YSZ powder has a constant mass for all temperatures and is hence not reduced (Fig. 1, dotted light grey line). The mass loss observed for the NiO/YSZ powder is therefore attributed solely to the NiO. The mass loss curve for the dense of NiO/YSZ sample (Fig. 1, dashed grey line) agrees with reports from similar experiments on dense samples [11,12,14]. It also shows the same overall trend as observed for the NiO/YSZ powder, except that the onset of the reaction is shifted up by ca. 100°C.
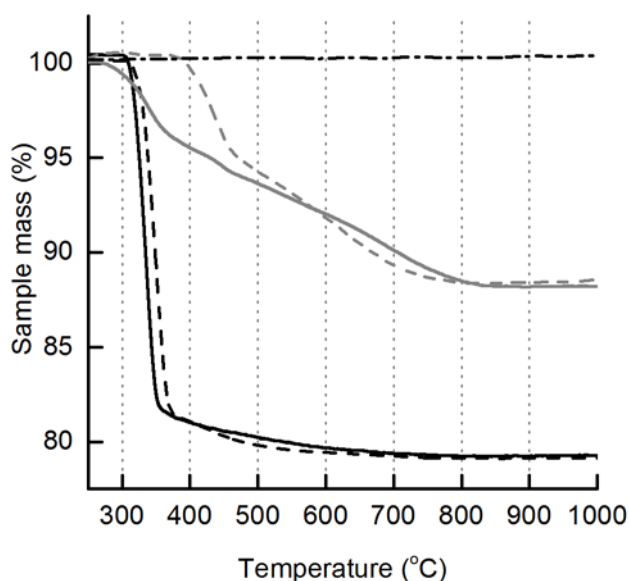
Fig. 1: The mass as a function of temperature for non-sintered NiO powder (solid black), NiO powder ground after sintering at 1350°C (dashed black), NiO/YSZ powder ground after sintering at 1350°C (solid grey), a dense piece of the NiO/YSZ sintered at 1350°C (dashed grey) and YSZ powder ground after sintering at 1350°C (black dash-dot) during exposure to 9% H_2/N_2 at a constant ramping rate of 1°C/min.

3.2 STEM-EDS results

As described in the introduction, it has been suggested that the inhibitive effect of YSZ could be partly explained by the formation of NiO crystallites incorporated in YSZ at high sintering temperatures and of a metastable solid solution of NiO in YSZ [16]. Previous studies have shown that nickel can enter YSZ during the sintering process [31,32]. STEM-EDS elemental maps of the NiO/YSZ powder sample were recorded in order to determine the spatial distribution of the Ni in the sample. Figure 2a shows typical a dark-field STEM image of an agglomerate of NiO and YSZ particles and Fig. 2b-d shows the spatial distribution of the Ni and Zr. Only a weak signal of Ni is observed in the area of the YSZ particles. Only areas that indicated a physical overlap of NiO and YSZ particles show stronger x-ray signals for both Ni and Zr. The analysis therefore shows a low degree of NiO incorporation in YSZ. Although incorporation of NiO into YSZ can partly explain a slower reduction of NiO, the small amount of Ni in the YSZ grains according to the STEM-EDS analysis shows that this is not likely the main explanation for the relatively strong inhibitive effect observed from TGA.
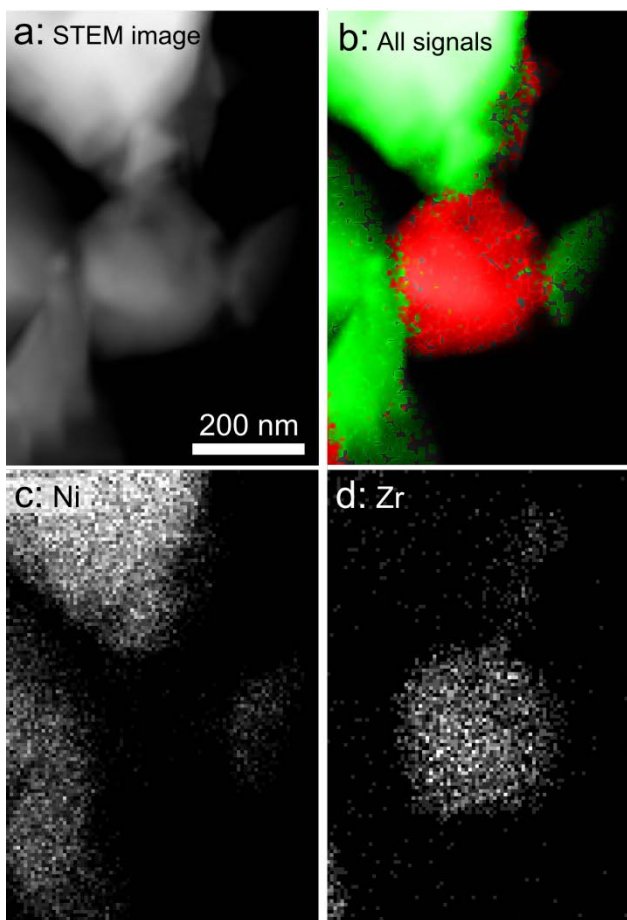
Fig. 2a-d: a) A HAADF STEM image, b) an elemental map (green = Ni, red = Zr), c) the spatial distribution of the Ni-Kα EDS signal, d) the spatial distribution of the Zr-Kα EDS signal of the NiO/YSZ powder sample.

3.3 Environmental TEM results

Figure 3 presents the reduction of the pure NiO powder inside the ETEM. The sample is exposed to 2 mbar H_2 while the temperature is ramped from 180°C by 1°C/min as in the TGA experiment (Fig. 1). At the relatively low magnification in Fig. 3, the lattice planes are not resolved, as when acquiring the image at higher resolution (See Fig. A.2 in the supplementary materials). Instead it can be seen that the NiO particle is initially dense, but apparently becomes porous, consistent with previous reports where the reduced Ni was characterized by a porous morphology [17-19]. The dense areas are therefore interpreted as NiO and the porous areas as Ni. For most of the recorded images series, the reduction was observed to initiate at several different sites at the NiO particles. The largest particle presented in Fig. 3 is a special case in the sense that the reduction initiated only at a few sites, e.g. at the site indicated by the arrow (Fig. 3b). It is observed that a front of porous Ni travels from the initial site over the NiO until the whole particle appears porous (See also the movie

"Low mag reduction of pure NiO powder" in the supplementary materials). According to Fig. 3, the reduction rate is therefore highest near the NiO-Ni interface, which illustrates the previously suggested autocatalytic effect for the NiO reduction [10]. Fig. 3 also illustrates an advantage of the in situ method compared to post mortem TEM analysis. In one experiment we are able to follow the reduction process from onset to full reduction. To produce an image series with a comparable temperature/time resolution by a series of aging treatments in a furnace combined with post mortem characterization would be much more time consuming. The heating and cooling between each step in the aging may influence the results. Such possible irreversible effects are avoided by the in situ experiment.
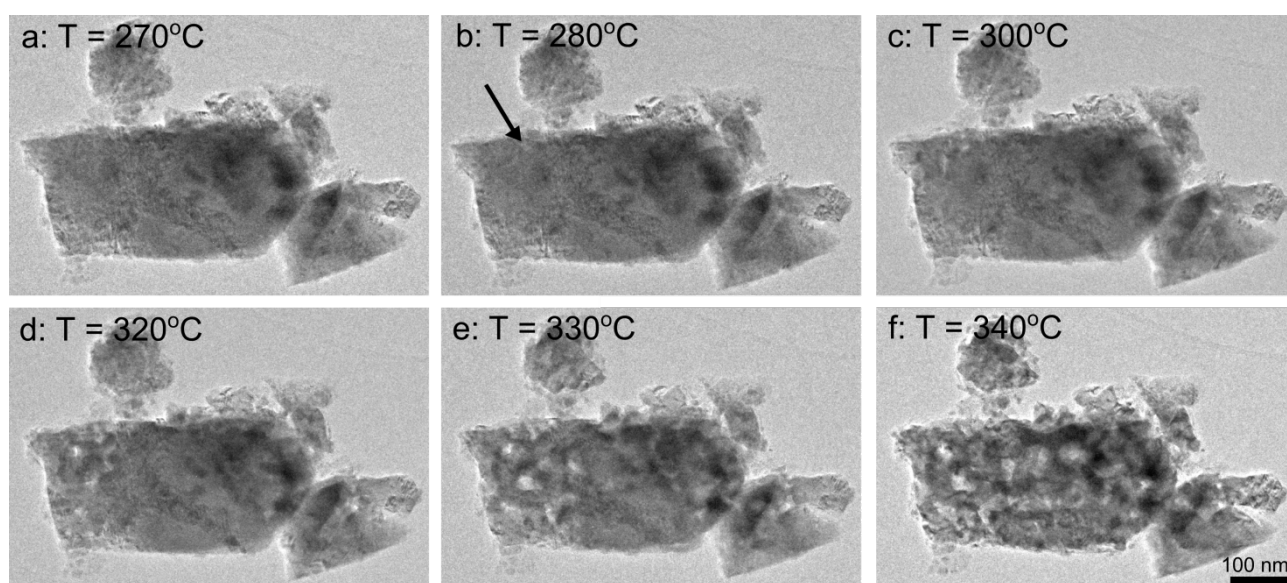

Fig. 3a-f: *In situ* TEM image series of the same region of the NiO powder sample during exposure to 2 mbar H_2 and constant temperature ramping rate of 1°C/min. To guide the eye, an arrow points to the site where close inspection reveals the first pore formation.

Figure 4 presents an ETEM image series of NiO/YSZ powder during exposure to 2 mbar H_2 while ramping the temperature at 1°C/min similar to the TGA experiment (Fig. 1) and to the *in situ* experiment for pure NiO (Fig. 3). As for the pure NiO, the reduction process of NiO in NiO/YSZ can be observed by the formation of a porous structure in the initially dense NiO (See also the movie "Low mag reduction of NiO/YSZ powder" in the supplementary materials). To guide the eye the initial reduction sites are indicated in Fig. 4b. It is observed that the reduction process is initiated near both NiO-gas and NiO-YSZ interfaces. No significant difference in the initiation and progression of the porous Ni reaction fronts could be identified in NiO close to or far from the NiO-YSZ interfaces. This result is representative of all six images series recorded of the NiO/YSZ

powder. From Fig. 4 it can be seen that the developed porous structure of Ni densified as the temperature is increased above 400°C. Densification of porous Ni at temperatures above 600°C has also been reported in a previous study on a NiO powder [26]. The observation is consistent with the suggested rule that metallic mobility in a hydrogen atmosphere is initiated approximately at the Tamman temperature, which for bulk Ni is 590°C [33].
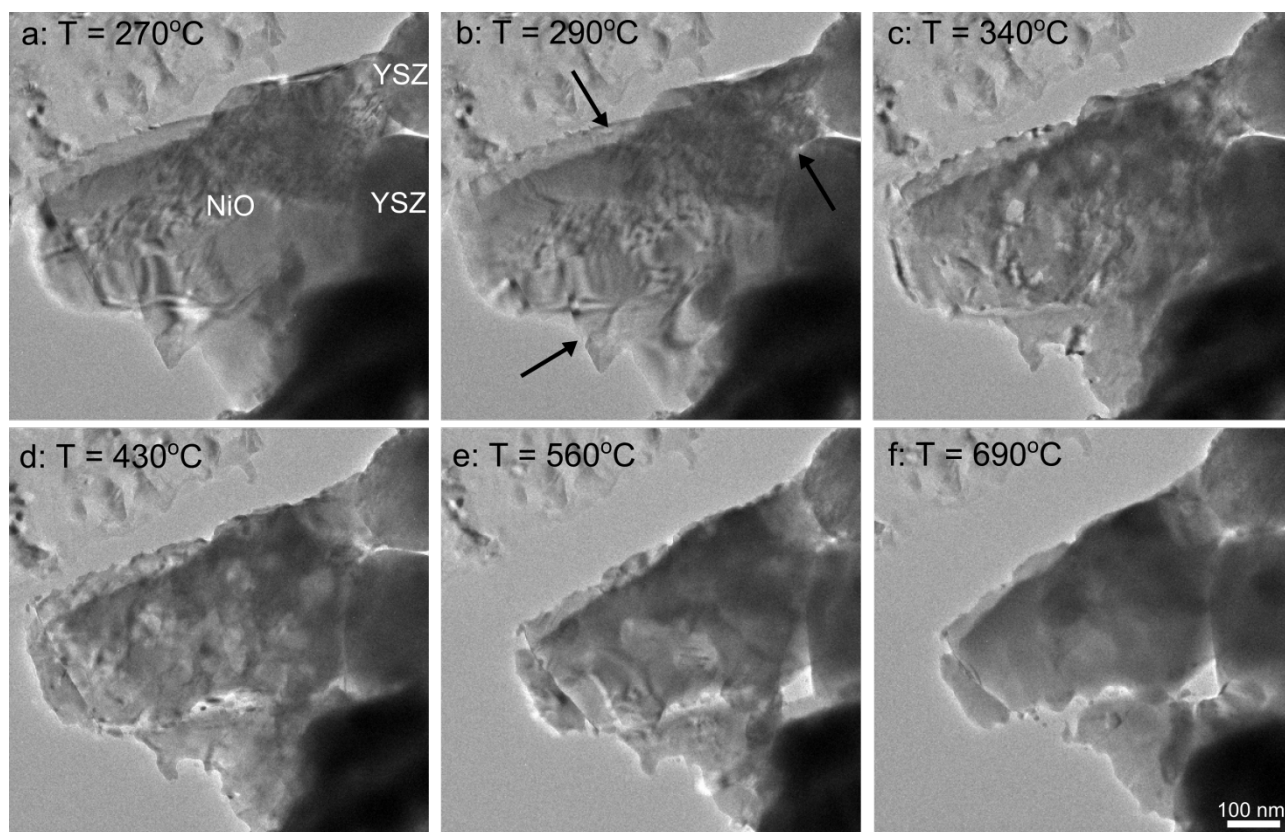

Fig. 4a-f: ETEM image series of the same region of the NiO/YSZ powder sample during exposure to 2 mbar H_2 and constant temperature ramping rate of 1°C/min. (a-c) presents the NiO reduction process. (d-f) presents the densification of reduced Ni at high temperatures. To guide the eye, an arrow points to the site where close inspection reveals the first pore formation.

In addition to ETEM image series, a series of electron diffraction patterns were recorded for each reduction experiment of NiO and NiO/YSZ (See Fig. A.3 in the supplementary materials). Fig. 5a illustrates the detailed temperature dependence of the electron diffraction signal: Here the normalized peak intensity of the NiO signal is presented as a function of temperature for NiO powder (black squares) and NiO/YSZ powder (grey squares). Comparison with the TGA data (NiO powder: black dashed line, NiO/YSZ: grey dashed line) shows that the temperature dependence determined from TEM of both NiO and NiO/YSZ matches the trend found from TGA for the pure

NiO powder (Fig. 5a). A similar analysis performed on a Ni reflection (not presented) was consistent with the presented analysis for the NiO reflection.

To compare the image and diffraction analysis as a function of temperature, the porous areas (interpreted as reduced parts of the sample) were estimated and manually outlined by using the software ImageJ for three different NiO and NiO/YSZ particles as a function of temperature. Figure 5b presents the normalized non-porous areas as a function of temperature for NiO powder (black squares) and NiO/YSZ powder (grey squares). As observed from the diffraction analysis (Fig. 5a), the temperature dependence of the reduction process of both NiO and NiO/YSZ matches the trend found from TGA for the NiO powder (Fig. 5b). In other words, YSZ does not inhibit the reduction of the thin NiO and NiO/YSZ TEM samples as it does for the macroscopic samples. Figure 5a-b also show that the image and diffraction analysis are consistent in the description of the temperature dependence of the reduction and verify that the pore formation is a good indicator of Ni formation.
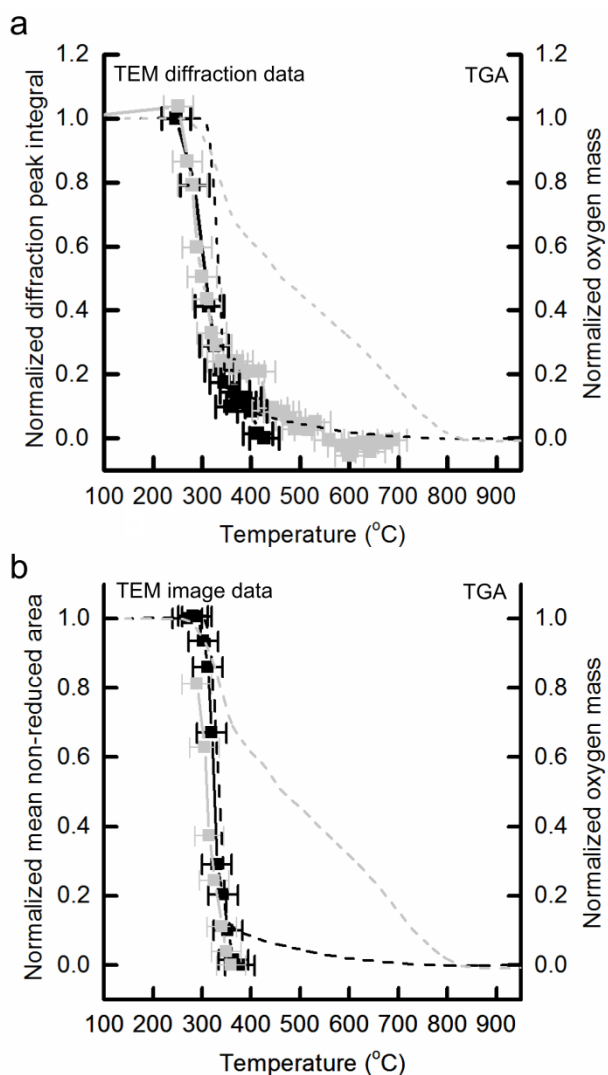
Fig. 5a-b: (a) Normalized electron diffraction peak integral for the NiO [440] peak for NiO powder (black squares) and NiO/YSZ powder (grey squares) presented as a function of temperature. (b) The normalized mean area of non-reduced NiO for three grains from a NiO powder (black squares) and NiO/YSZ powder (grey squares) presented as a function of temperature. For comparison, the TGA data of the normalized oxygen mass for NiO powder (black dotted line) and NiO/YSZ powder (grey dotted line) from Fig. 1 is presented. Error bars indicate the estimated errors on the temperature calibration.

In order to address the Ni mobility at high temperatures (>400°C) as indicated in Fig. 4d-f, an experiment was designed to study the reduction of NiO/YSZ when exposed to H_2 instantly at a realistic operation temperature near 800°C. The ideal way of performing such an experiment would be to ramp the temperature to the operation temperature in an inert gas and record the response from the sample when H_2 is introduced at the high temperature. To do this a new calibration of the TEM heating chip would be needed for the inert gas, and changing the gas composition in this way would, however, simultaneously influence the temperature of the sample. In practice, the NiO/YSZ powder was exposed to H_2 at room temperature and the temperature was ramped to 780°C with the high ramping rate of 1000°C/s. In this way the environment is changed from non-reducing, to reducing at 780°C in 1 s. Figure 6a-c presents a TEM image series of the experiment. The first image (Fig. 6a) presents the sample in H_2 at room temperature and the second image (recorded 2 s later) presents the sample in H_2 at 780°C. The figure shows that the sample structure changes abruptly during the short reduction time and that only slower changes take place after the first 2 s for the nanoscaled structure (Fig. 6b-c). None or only minor sample porosity is observed and the sample appears to directly transform into the dense state. Therefore it is not possible from the image series to uniquely identify the location of the NiO and the YSZ particles, except by assuming that only the shape of the Ni and not the YSZ particles are changed at this temperature.
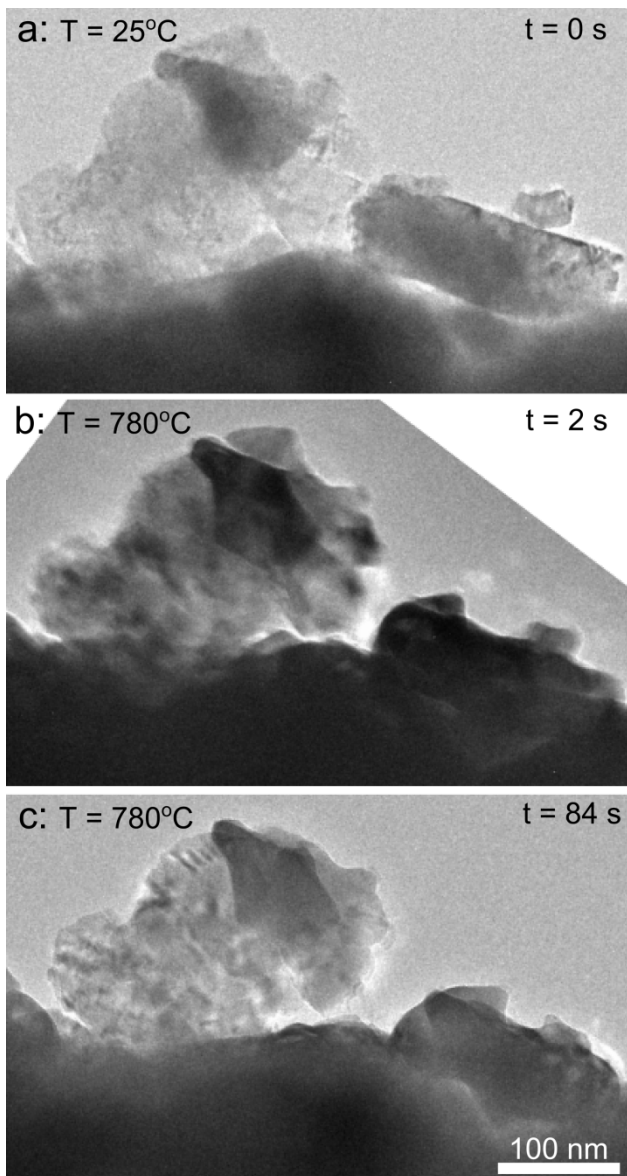
Fig. 6a-c: *In situ* TEM image series of the same region of the NiO/YSZ powder during exposure to 2 mbar H_2. The temperature is ramped by 1000°C/s between image (a) and (b) and held constant hereafter. The time of the image acquisition and the temperature is indicated in each image. The dark contrast of the sample in (b) relative to (a, c) is due to an abrupt change in focus during temperature ramping, which was adjusted in (c).

4. Discussion

According to the TGA results, the reduction reaction of NiO with H_2 is generally slower for NiO/YSZ powder or dense samples compared to the reduction of pure NiO powders (Fig. 1). This result is consistent with results from previous studies where it was suggested that YSZ has an inhibitive effect on the NiO reduction [11,12,16]. The samples from references [12,16] are relatively comparable to the present samples ([16]: dense samples prepared by mixing 60 mol%

NiO/YSZ with 8 mol% yttria, die pressed and sintering in air, at temperatures of 1400°C or 1600°C for 2 or 8 hours respectively, [12]: dense or powder samples prepared by mixing 65 mol% NiO/YSZ with 8 mol% yttria, die pressed and sintering in air, at temperatures of 1200 - 1400°C for 5 hours). It has been suggested that the NiO reduction is inhibited directly by YSZ at or near the NiO/YSZ interface, e.g. via strong NiO-YSZ chemical interaction [16] or due to slow Ni nucleation at the NiO-YSZ interface [12]. Such direct NiO-YSZ interactions as well as mass/gas transport limitations are likely to influence the NiO reduction rate, but the degree of influence from these different phenomena is still not clear. It is therefore interesting that no inhibitive effect is observed with ETEM (Fig. 5), but only with TGA for the same type of sample (Fig. 1) in the present study. Also, in a recent ETEM study of a dense planar NiO/YSZ sample, which was thinned by a focused ion beam, the inhibitive effect from YSZ on NiO reduction was not observed [19]. This study even suggests that the NiO reduces slightly faster at a NiO-YSZ interface than at a NiO-gas phase interface, but this could not be observed in the present ETEM experiments (Fig. 4 and Fig. 5). It is important to note that the results from studies of macroscopic samples are influenced by e.g. mass and gas transport limitations depending on the structure of the three-dimensional network of NiO, YSZ and pores in the sample. On the contrary, TEM samples do not form such a three-dimensional framework, but are almost two-dimensional with a thickness up to only a few hundred nanometers where each particle has access to the gas phase. It can therefore be expected that mass and gas transport limitation will only have minor influence on the reaction rates observed from ETEM. This could indicate that the inhibitive effect of YSZ on the NiO reduction observed from TGA is mainly due to limitations of mass and/or gas transport.

It should be emphasized that the comparison of the present results with previous works may be partly hampered by the variations in SOFC/SOEC sample preparation since there is no universal standard cell material. Therefore NiO-YSZ-gas phase interactions could be influenced by such sample variations. For example the gas and mass transport is obviously different for powders and dense samples and higher sintering temperatures may lead to a higher degree of chemical NiO-YSZ interactions or to a higher degree of nickel incorporation in YSZ as for example observed in reference [31].

Besides presenting the reduction process of NiO/YSZ at the nanoscale, the ETEM experiments also show that the Ni is mobile at temperatures above ca. 400°C (Fig. 4). A high mobility was observed at 780°C, which is close to the normal operating temperature a solid oxide fuel or electrolysis cell

(Fig. 6). This suggests that the electrochemically active structures of the operating cell, the so-called triple phase boundaries between Ni (solid), YSZ (solid) and H_2 (gas), are dynamic at the nanoscale. The structure of the triple phase boundaries can therefore be expected to change during the lifetime of the cells leading to activation or more likely to deactivation depending on the developed structure.

The results from Fig. 6 also suggest that the reduction process near 800°C of an industrial SOFC (SOEC), will lead to immediate collapse of any Ni nanopores to form dense Ni particles. The larger micro-pores formed from the volume loss of oxygen during the reduction are, however maintained. This is partially due to the structure of YSZ, which is not changed by the reduction process [11], but even for initially dense samples of pure NiO, micro-porosity is observed after reduction in 100% H_2 at temperatures as high as 1000°C and the pore sizes increase with the reduction temperature [17,18]. Hidayat *et al.* found that at temperatures up to 600°C, NiO reduction was well-described by kinetics limited by the chemical reaction at the Ni-NiO interface contrary to kinetics limited by gas transport [18]. At higher temperatures the observed reaction rate was lower than suggested by the kinetic interface-limited model and a lower overall reaction rate was even observed at 600-800°C compared to the lower temperatures [17,18]. The authors suggest that this is related to the temperature dependent pore sizes, by a transition from the interface-limited reaction to kinetics limited by solid state diffusion of Ni cations in the NiO [18]. The conclusion was based on a model, which does not take the observed dynamical morphological changes of the Ni (Fig. 4, Fig. 6) into account. The present results suggest the alternative explanation that the larger pore sizes observed at high temperatures are due to collapse of the Ni nanopores and coarsening of the Ni particles (fig 4, Fig. 6). It is well-known that gas diffusion rates depend on the pore sizes, and such a structural change will therefore influence the overall reaction rates [34]. Besides changing the Ni pore structure, the mobility of the Ni could also lead to a high coverage of Ni on the NiO surface and thereby lower the access of the gas phase to the active sites. Further investigations are needed to determine if this is the case at the micro-scale during reduction in dry H_2. It has, however, already been reported, that a fully dense Ni layer can be created on top of NiO, by reducing at a high temperature while slowing down the reduction process by using a low H_2-to-H_2O ratio feed gas. After formation of the dense Ni layer, the reaction process slowly proceeds via diffusion of hydrogen through the Ni [18].

It should be emphasized that the model SOFC anode (SOEC cathode) used in the ETEM experiments in some respects will deviate from industrial anodes (cathodes). As described in detail in the methods section, the NiO/YSZ powder sample is not simply a mixture of NiO and YSZ powders, but is prepared from a sintered dense ceramic SOFC anode (SOEC cathode), which was thinned for TEM by breaking the sample into small agglomerates. As discussed above the mass and gas transport during reduction for such a ceramic powder sample can be expected to be different than compared to the initial dense ceramic. Figure 1 compares the reduction profiles for the powder (solid grey) and dense (dashed grey) NiO/YSZ, illustrating that the profiles indeed are different. It may be surprising to observe that the difference is mainly a shift in onset temperature, while similar reduction profiles are observed in the high temperature range from about 500°C and up. Several reasons for the temperature shift can be suggested: The preparation step of grinding the dense sample into powder will for example introduce additional defects at the NiO surfaces. As described in the introduction, the incubation period for NiO reduction scales with the number of NiO surface defects. Also, the powder sample has a significantly higher NiO surface area exposed directly to the gas phase. Further studies are needed to determine the most important reasons. When comparing the reduction of nanoscaled ceramic powder samples with industrial SOFC anodes (SOEC cathodes) these differences should therefore be taken into account.

It should also be mentioned that despite the difference in the H_2 pressure of almost a factor of 50 in the ETEM experiment compared to the TGA experiment, the reduction onset temperature of the NiO powders did not shift. This may seem surprising when taking into account the previously reported dependence of the reaction rate on the H_2 partial pressure [8,10,17]. These reports are, however, based on comparison of different pressure regimes (10^{-7} – 7 mbar [8,10] and 260 – 1000 mbar [17]) and may not be comparable to the present conditions. An additional TGA experiment was performed for the non-sintered NiO powder sample in 0.2% H_2/N_2, comparable to the H_2 partial pressure in the ETEM experiment and with slow temperature ramping of 0.1 °C/min. Also for this experiment the temperature onset for NiO reduction was ca. 300°C (not presented).

5. Conclusions

The reduction process of NiO and NiO/YSZ was investigated by the comparison of results from ETEM and TGA. The TGA results showed the inhibitive effect from YSZ. ETEM images and the diffraction series revealed nanoscaled pore formation of NiO and NiO/YSZ during the reduction above 280°C. It was also found that the inhibitive effect from YSZ is not due to a direct local

interaction between NiO and YSZ. Instead it is suggested that the effect results from gas and/or mass transport limitations in the complex three-dimensional structure of the SOFC anode/SOEC cathode. These limitations may be taken into account when designing new reduction procedures for optimizing the performance of the electrochemical cells. It may also be taken into account that the reduced Ni was observed to be mobile at temperatures above 400°C and rapid mobility at the nanoscale was observed near normal operation temperatures for an industrial SOFC/SOEC. This means that the nanoscaled three-dimensional structures of an SOFC/SOEC can vary significantly depending on the reduction and operation temperatures. Specifically, nanoporosity in the Ni particles will decay for temperatures above 400°C. The observed Ni mobility also confirms that electrochemical cells suffer from deactivation due to coarsening of Ni at the triple-phase boundaries.

References

1. H. Knozinger, E. Taglauer, in: G. Ertl, H. Knözinger, J. Weitkamp (Eds), Handbook of Heterogeneous Catalysis, vol. 3, Wiley-VCH, New York, 1997, pp. 216-231.

2. B. Delmon, in: G. Ertl, H. Knözinger, J. Weitkamp (Eds), Handbook of Heterogeneous Catalysis, vol. 3, Wiley-VCH, New York, 1997, pp. 264-285.

3. V.R. Choudhary, A.M. Rajput, A.S. Mamman, J. Catal. 178 (1998) 576-585.

4. L.A. Bruce, J.F. Mathews, Appl. Catal. 4 (1982) 353-370.

5. S.B. Simonsen, D. Chakraborty, I. Chorkendorff, S. Dahl. Appl. Catal. A-Gen, 447– 448 (2012) 22– 31.

6. A.F. Benton, P.H. Emmett, J. Am. Chem. Soc. 46 (1924) 2728-2737.

7. G. Parravano, J. Am. Chem. Soc. 74 (1952) 1194-1198.

8. R.P. Furstenau, G. McDougall, M.A. Langell, Surf. Sci. 150 (1985) 55-79.

9. E.C. Dickey, V.P. Dravid, P.D. Nellist, D.J. Wallis, S.J. Pennycook, A. Revcolevschi, Microsc. Microanal. 3 (1997) 443-450.

10. J.A. Rodriguez, J.C. Hanson, A.I. Frenkel, J.Y. Kim, M. Perez, J. Am. Chem. Soc. 124 (2002) 346-354.

11. H. Mori, C. Wen, J. Otomo, K. Eguchi, H. Takahashi, Appl. Catal. A-Gen. 245 (2003) 79-85.

12. D. Fouquet, A.C. Müller, A. Weber, E. Ivers-Tiffée, Ionics 8 (2003) 103-108.

13. N.M. Tikekar, T.J. Armstrong, A.V. Virkar, in: S.C. Singhal, M. Dokiya (Eds), Electrochemical Society Proceedings vol. 2003-07, The Electrochemical Society Inc., Pennington, 2003, pp. 670-679.

14. D. Waldbillig, A. Wood, D.G. Ivey, Solid State Ionics 176 (2005) 847-859.

15. A. Hagen, H.F. Poulsen, T. Klemensø, R.V. Martins, V. Honkimäki, T. Buslaps, R. Feindenhans'l, Fuel Cells 5 (2005) 361-366.

16. N.M. Tikekar, T.J. Armstrong, A.V. Virkar, J. Electrochem. Soc. 153 (2006) A654-A663.

17. T. Hidayat, M.A. Rhamdhani, E. Jak, P.C. Hayes, Metall. Mater. Trans. B 40B (2009) 1-16.

18. T. Hidayat, M.A. Rhamdhani, E. Jak, P.C. Hayes, Metall. Mater. Trans. B 40B (2009) 474-489.

19. Q. Jeangros, A. Faes, J.B. Wagner, T.W. Hansen, U. Aschauer, J. Van Herle, A. Hessler-Wyser, R.E. Dunin-Borkowski, Acta Mater. 58 (2010) 4587-4589.

20. S.L. Ebbehøj, T. Ramos, M. Mogensen, ECS Trans. 45 (2012) 363-375.

21. R.T.K. Baker, P.S. Harris, J. Phys. E Sci. Instrum. 5 (1972) 793-797.

22. R. Sharma, P.A. Crozier, in: N. Yao, Z.L. Wang (Eds.), Handbook of Microscopy for Nanotechnology, Klüwer Academic Publishers, Boston/Dordrecht/New York/London, 2005, pp 531-565.

23. P.L. Hansen, S. Helveg, A. Datye, Adv. Catal. 50A (2006) 77–94.

24. B. Wagner, F. Cavalca, C.D. Damsgaard, L.D.L. Duchstein, T.W. Hansen, Micron 43 (2012) 1169–1175.

25. S. Chenna, R. Banerjee, P.A. Crozier, Chem. Cat. Chem. 3 (2011) 1051-1059.

26. Q. Jeangros, T.W. Hansen, J.B. Wagner, C.D. Damsgaard, R.E. Dunin-Borkowski, C. Hébert, J. Van Herle, A. Hessler-Wyser, 10th European SOFC Forum proceedings (2012) B0503.

27. S. Chenna, P.A. Crozier, Micron 43 (2012) 1188-1194.

28. R. Banerjee. P.A. Crozier, J. Phys. Chem. C 116 (2012) 11486−11495.

29. S. Ramousse, M. Menon, K. Brodersen, J. Knudsen, U. Rahbek, P.H. Larsen, ECS Trans. 7 (2007) 317-327.

30. T.W. Hansen, J.B. Wagner, R.E. Dunin-Borkowski, Mater. Sci. Technol. 26 (2010) 1338-1344.

31. D.L. King, J.J. Strohm, X. Wang, H.-S. Roh, C. Wang, Y.-H. Chin, Y. Wang, Y. Lin, R. Rozmiarek, P. Singh, J. Catal. 258 (2008) 356-365.

32. A. Kuzjukevics, S. Linderoth, Solid State Ionics 93 (1997) 255-261.

33. R.T.K. Baker, J. Catal. 78 (1982) 473-476.

34. J.M. Thomas, W.J. Thomas, Principles and practice of heterogeneous catalysis, VCH, Weinheim, 1997, pp. 290-314.

List of figure captions

Fig. 1: The mass as a function of temperature for non-sintered NiO powder (solid black), NiO powder ground after sintering at 1350°C (dashed black), NiO/YSZ powder ground after sintering at 1350°C (solid grey), a dense piece of the NiO/YSZ sintered at 1350°C (dashed grey) and YSZ powder ground after sintering at 1350°C (black dash-dot) during exposure to 9% H_2/N_2 at a constant ramping rate of 1°C/min.

Fig. 2a-d: a) A HAADF STEM image, b) an elemental map (green = Ni, red = Zr), c) the spatial distribution of the Ni-Kα EDS signal, d) the spatial distribution of the Zr-Kα EDS signal of the NiO/YSZ powder sample.

Fig. 3a-f: *In situ* TEM image series of the same region of the NiO powder sample during exposure to 2 mbar H_2 and constant temperature ramping rate of 1°C/min. To guide the eye, an arrow points to the site where close inspection reveals the first pore formation.

Fig. 4a-f: ETEM image series of the same region of the NiO/YSZ powder sample during exposure to 2 mbar H_2 and constant temperature ramping rate of 1°C/min. (a-c) presents the NiO reduction process. (d-f) presents the densification of reduced Ni at high temperatures. To guide the eye, an arrow points to the site where close inspection reveals the first pore formation.

Fig. 5a-b: (a) Normalized electron diffraction peak integral for the NiO [440] peak for NiO powder (black squares) and NiO/YSZ powder (grey squares) presented as a function of temperature. (b) The normalized mean area of non-reduced NiO for three grains from a NiO powder (black squares) and NiO/YSZ powder (grey squares) presented as a function of temperature. For comparison, the TGA data of the normalized oxygen mass for NiO powder (black dotted line) and NiO/YSZ powder (grey dotted line) from Fig. 1 is presented. Error bars indicate the estimated errors on the temperature calibration.

Fig. 6a-c: *In situ* TEM image series of the same region of the NiO/YSZ powder during exposure to 2 mbar H_2. The temperature is ramped by 1000°C/s between image (a) and (b) and held constant hereafter. The time of the image acquisition and the temperature is indicated in each image. The dark contrast of the sample in (b) relative to (a, c) is due to an abrupt change in focus during temperature ramping, which was adjusted in (c).

Appendix A. Supplementary material

ETEM movies

"Low mag reduction of pure NiO powder"

The movie shows the same region of the NiO powder sample during exposure to 2 mbar H_2 and constant temperature ramping rate of 1°C/min. The temperature is indicated in each frame.

"Low mag reduction of NiO/YSZ powder"

The movie shows the same region of the NiO/YSZ powder sample during exposure to 2 mbar H_2 and constant temperature ramping rate of 1°C/min. The temperature is indicated in each frame.

Temperature calibration of the ETEM heating chips

The temperature in the gas environment was calibrated using melting points of Zn nanoparticles (diameter = ca. 100-300 nm, melting point is approximately equal to the bulk melting point of ca. 420°C [L. Gunawan, G.P. Johari, J. Phys. Chem. C 112 (2009) 20159-20166]) and Ag nanoparticles (diameter = ca. 20 nm, melting point ca. 900°C [W. Luo, W. Hu, S. Xiao, J. Phys. Chem. C 112 (2008) 2359-2369.]) dispersed on E-chips with a SiN support film. Here the temperature was ramped in steps of 25°C by 50°C/s and for each step maintained constant for 2 min to record an electron powder diffraction pattern of the sample. The melting point was determined by the disappearance of diffraction spots with an estimated error of 25°C, and it was verified that the spots returned when the temperature was lowered below the melting point. The melting points were also determined for the two metals in vacuum (10^{-6} mbar) and were found to correspond to the reference melting points for the metal nanoparticles, thereby verifying the initial calibration from the supplier. The resulting temperature calibration curve is based on a polynomial fit to three points (the melting points for Zn and Ag and additionally the point at room temperature) (Fig. A.1).
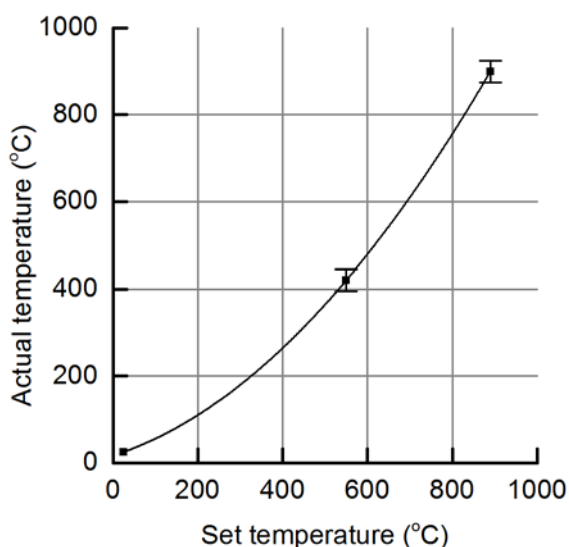

Fig. A.1: The actual temperature in 2 mbar H_2 of the MEMS electrical TEM heating chip is presented as a function of the set temperature. The equation for the polynomial fit is: $7.6 \cdot 10^{-4} x^2 + 0.31x + 16.7$.

In situ HRTEM

Figure A.2a-f presents a HRTEM image series of the NiO/YSZ powder during exposure to 2 mbar H_2 at the constant temperature of 320°C. Crystals of NiO and Ni were identified in the HRTEM images from the characteristic lattice plane distances for the two phases as indicated in the figure

(Fig. A.2a-f). In addition to Ni and NiO, sheets of graphitic carbon are also observed on the surface of one of the Ni crystals and identified from the characteristic lattice spacing for graphite (Fig. A.2a-f). Carbon formation on Ni catalysts is a well-known phenomenon [See for example E.G.M. Kuijpers, J.W. Geus, Fuel 62 (1983) 158-161.]. The carbon is present on the sample since the samples were exposed to air prior to the ETEM analysis. In addition, the image series shows that the growth of Ni crystals is accompanied by shrinkage of the NiO crystals. The observations are consistent with a reduction process of NiO into pure Ni.
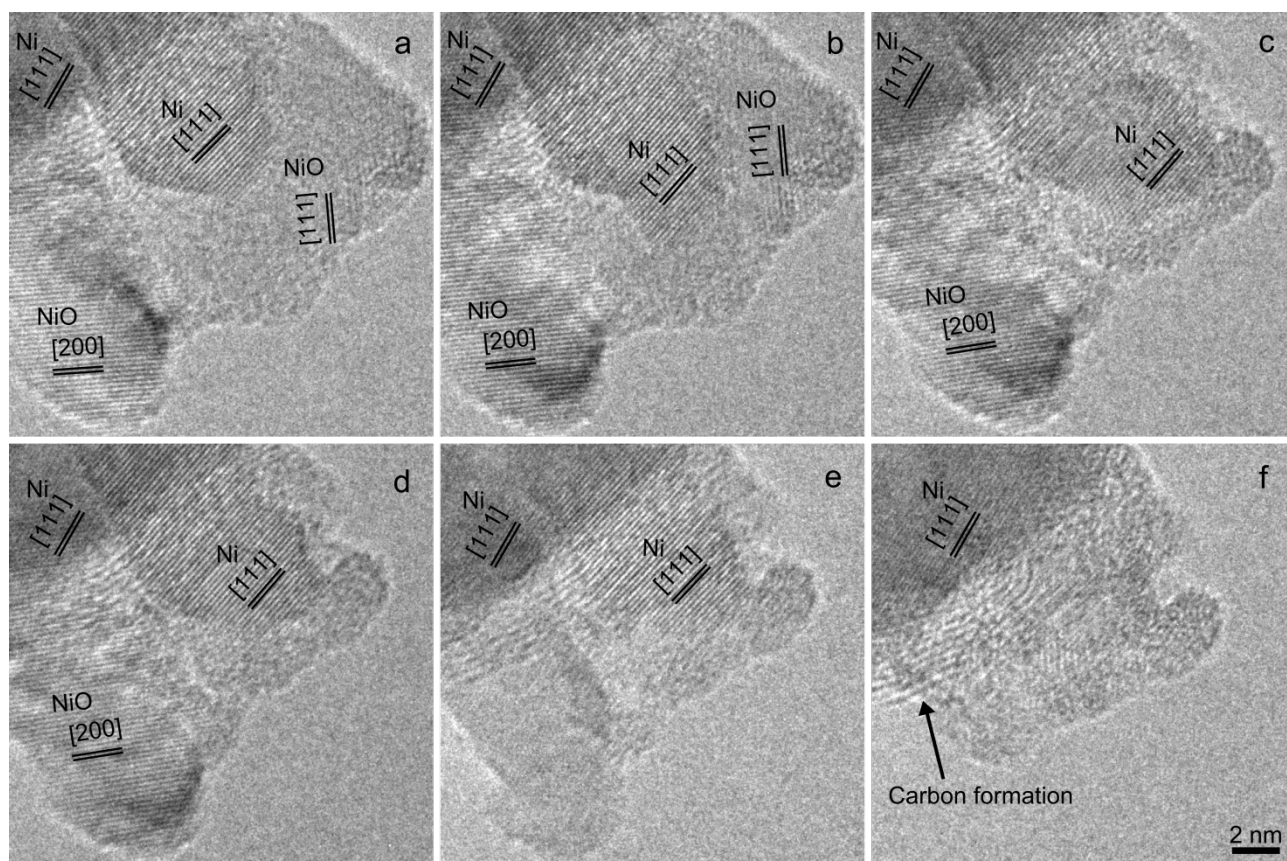

Fig. A.2a-f: In situ HRTEM image series of the same region of a NiO/YSZ powder sample during exposure to 2mbar H_2 at 320°C. The waiting time between each image is 10s. Identified lattice distances for Ni and NiO are indicated. Carbon formation at the Ni surface is seen in all images (a-f) and its location is indicated in (f).

ETEM electron powder diffraction

Examples of powder diffraction images recorded during the ETEM reduction of NiO and NiO/YSZ are presented by Fig. A.4. The diffraction patterns were recorded during the same experiments as those presented by Fig. 5 and fig 6. As indicated in the Fig. A.3, the patterns recorded at room

temperature resemble the NiO phase for both samples (Fig. A.3a,c) and the patterns recorded at 650°C in H_2 resemble the Ni phase for both samples (Fig. A.3b,d).
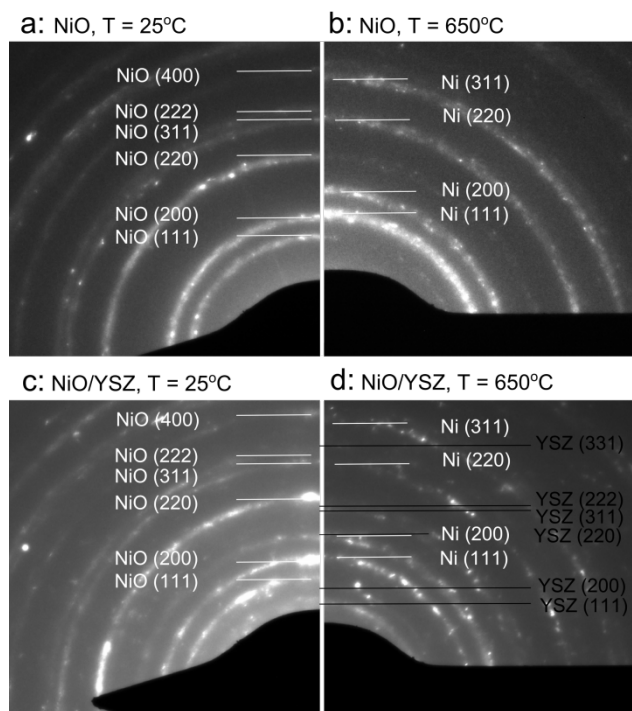

Fig. A.3a-d: Diffraction patterns recorded over the relatively large region of ca. 4 μm² during exposure to 2mbar H_2 for (a-b) NiO powder and for (b-c) NiO/YSZ powder at the temperature of (a,c) 25°C and (c,d) 560°C. Reference distances for Ni, NiO and YSZ lattice planes are indicated.

X-ray diffraction (XRD)

XRD measurements were performed on the powder samples on a Bruker D8 Advance diffractometer using the Cu Kα1 radiation in the range of $2\theta = 20\text{-}90°$. Figure A.4 presents the XRD results. The patterns show that the NiO phase in the NiO/YSZ is identical to that of pure NiO and that the YSZ phase in the NiO/YSZ is identical to that of pure YSZ. The NiO and YSZ patterns also match reference spectra (not presented) for the two pure phases.
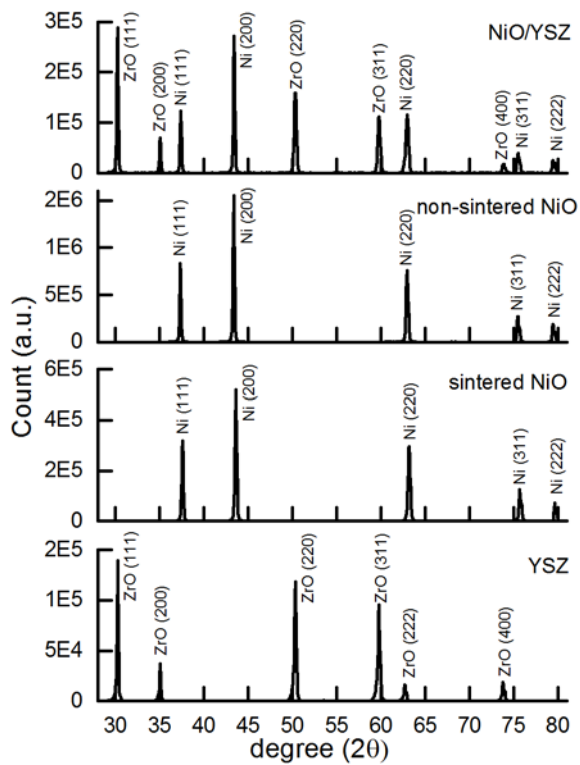
Fig. A.4: XRD spectra of the non-sintered NiO powder, NiO powder ground after sintering at 1350°C, NiO/YSZ powder ground after sintering at 1350°C and YSZ powder ground after sintering at 1350°C.